BIOENGINEERING

Microfluidic device for the formation of optically excitable, three-dimensional, compartmentalized motor units

Sebastien G. M. Uzel,[1] Randall J. Platt,[2,3] Vidya Subramanian,[4] Taylor M. Pearl,[2] Christopher J. Rowlands,[2] Vincent Chan,[1] Laurie A. Boyer,[4] Peter T. C. So,[1,2,5] Roger D. Kamm[1,2,5]*

Motor units are the fundamental elements responsible for muscle movement. They are formed by lower motor neurons and their muscle targets, synapsed via neuromuscular junctions (NMJs). The loss of NMJs in neurodegenerative disorders (such as amyotrophic lateral sclerosis or spinal muscle atrophy) or as a result of traumatic injuries affects millions of lives each year. Developing in vitro assays that closely recapitulate the physiology of neuromuscular tissues is crucial to understand the formation and maturation of NMJs, as well as to help unravel the mechanisms leading to their degeneration and repair. We present a microfluidic platform designed to coculture myoblast-derived muscle strips and motor neurons differentiated from mouse embryonic stem cells (ESCs) within a three-dimensional (3D) hydrogel. The device geometry mimics the spinal cord–limb physical separation by compartmentalizing the two cell types, which also facilitates the observation of 3D neurite outgrowth and remote muscle innervation. Moreover, the use of compliant pillars as anchors for muscle strips provides a quantitative functional readout of force generation. Finally, photosensitizing the ESC provides a pool of source cells that can be differentiated into optically excitable motor neurons, allowing for spatiodynamic, versatile, and noninvasive in vitro control of the motor units.

INTRODUCTION

Motor units, consisting of lower motor neurons (MNs) and the muscle fibers that they innervate via neuromuscular junctions (NMJs), are the fundamental elements responsible for producing virtually all motor functions, from locomotion to respiration or speech. Their failure is associated with highly incapacitating or lethal genetic disorders, such as amyotrophic lateral sclerosis (ALS), spinal muscle atrophy (SMA), or Duchenne muscular dystrophy (DMD) (*1*), or traumatic injuries. Serving as a model for synaptic function, motor units have been the object of previous pioneering work that led to the identification of neurotransmitters and their quantal release (*2*, *3*). In vertebrates, NMJ function involves numerous specialized cell types, from astrocytes secreting supporting factors to Schwann cells providing electrical and chemical isolation (*4*, *5*). Commonly used primitive animal models, such as aplysia, *Caenorhabditis elegans*, or *Drosophila* larva, provide important but limited insight into the physiology of vertebrate and mammalian NMJs due to fundamental differences in these models, such as the absence of synapse elimination and remodeling, the presence of glutamatergic MNs or inhibitory NMJs, and the absence of myelin sheath (*6*–*8*). On the other hand, mammalian in vivo models are complex and not amenable to systematic parameter tuning.

Development of in vitro systems that mimic their in vivo counterparts and allow for de novo NMJ formation therefore remains a high priority. Traditional two-dimensional (2D) culture platforms, advantageous for their simplicity, typically consist of a layer of myotubes differentiated from myoblasts onto which MNs are uniformly plated (*9*–*17*). These 2D mixed culture systems, using various combinations of human, rodent, or chick cells, have been used for decades and have contributed greatly to our understanding of the fundamental physiology of NMJs; examples include acetylcholine receptor (AChR) clustering (*9*), the role of Schwann cells on NMJ formation (*10*), or the regulation of acetylcholinesterase activity (*11*). They have also proven to be efficient tools to investigate the functionality of healthy (*12*, *13*) and dysfunctional (*14*) stem cell–derived MNs and have served to optimize in vitro neuron/muscle culture conditions (*15*–*17*).

However, their simplicity can, at times, be outweighed by their limitations. The 2D nature of the system leads to a mismatch between the mechanical properties of the cells and the substrate that can impede muscle differentiation (*18*) or affect neurite outgrowth (*19*, *20*) and preclude direct interaction between the extracellular matrix (ECM) and the resident neurons and muscle cells (*21*, *22*). The mixed nature of the cultures makes it difficult to monitor individual cell types or axonal outgrowth and hinders the proper supply of tissue-specific factors or drugs. Moreover, the contraction generated by the muscle tissue can only be qualitatively assessed. Finally, these traditional platforms do not favor high throughput and limit scientists' ability to automate cell handling and data acquisition.

Over the years, progress has been made toward addressing some of these limitations associated with the traditional assays. Campenot chambers (*23*) have been used for compartmentalized 2D cocultures to study synapse elimination (*24*) or allow for enhanced visualization of axonal outgrowth (*25*). Microfluidic devices confer a higher throughput while increasing manipulability and control over culture conditions and have been proposed and applied to remotely innervate cardiac cells with autonomic neurons (*26*, *27*) or skeletal muscle cells with MNs (*28*–*31*). Other systems enable culture in a 3D configuration in an attempt to increase the physiological relevance. They take the form of organotypic spinal cord slices in contact with myoblast-laden fibrin gels (*32*) or microdevices inspired by 3D muscle culture systems

[1]Department of Mechanical Engineering, Massachusetts Institute of Technology (MIT), Cambridge, MA 02139, USA. [2]Department of Biological Engineering, MIT, Cambridge, MA 02139, USA. [3]Broad Institute of MIT and Harvard, Cambridge, MA 02142, USA. [4]Department of Biology, MIT, Cambridge, MA 02139, USA. [5]BioSystems and Micromechanics (BioSyM) IRG, Singapore-MIT Alliance for Research and Technology, Singapore, Singapore.
*Corresponding author. Email: rdkamm@mit.edu

(*33*, *34*), allowing the formation of 3D muscle bundles onto which MN-containing neurospheres were seeded (*35*). However, these configurations lacked clear physical separation between cell types. Finally, some platforms have used compliant substrates to quantitatively infer muscle contraction, whether by plating the cells on arrays of microneedles (*36*), flexible membranes (*37*), or silicon cantilevers (*38*, *39*). This latter concept was the basis for a study that reported the formation of functional NMJ between MNs and muscle cells plated onto these cantilevers and the high-throughput and quantitative assessment of neuromuscular physiology and drug response (*40*).

Here, we present an in vitro platform that is made more "physiologically relevant" by allowing simultaneous 3D coculture and compartmentalization of mouse embryonic stem cell (mESC)–derived MNs and skeletal muscle cells within an ECM. This platform capitalizes on microfluidic designs for 3D cell culture (*41*–*43*) and the use of passive force transducers for quantitative measurement of muscle contraction (*44*, *45*) [reviewed in the study by Uzel *et al.* (*46*)]. The system enables the culture of functional differentiated MNs and myofibers, the observation of 3D axonal outgrowth with the hydrogel, and the formation of functional NMJs.

To facilitate MN excitation and provide a means of rapid, spatially resolved and noninvasive MN activation, we use the optically excitable cation channel Channelrhodopsin-2 (ChR2). ChR2 and other opsins of the same family have proven to be valuable and versatile tools in neuroscience (*47*, *48*) and have been widely used in in vivo models to stimulate NMJs (*49*–*52*). Here, we photosensitize an mESC line with an optimized ChR2 ($ChR2^{H134R}$) and subsequently differentiate these cells into MNs to optically induce action potentials (APs) and interrogate the NMJ. This method, recently applied to ESCs overexpressing glia-derived neurotrophic factors (GDNFs) for enhanced survival (*53*) and even more recently to human induced pluripotent stem (iPS) cells (*54*), foreshadows how any pluripotent cell lines (a fortiori patient-derived iPS cells) can provide consistent optogenetically modified MNs. After characterizing the optogenetic targeting of the ESC and the optical excitability of the $ChR2^{H134R}$-ESC–derived MNs, we demonstrate their ability to trigger the contraction of muscle cells first in a traditional dish assay, as well as in our new 3D compartmentalized microfluidic device.

RESULTS

$ChR2^{H134R}$-expressing mESCs differentiate into light-activatable MNs

Photosensitization of the mESC line HBG3 [expressing cytosolic green fluorescent protein (GFP) under the control of the MN-specific Hb9 promoter] was carried out by knocking in tdTomato-tagged $ChR2^{H134R}$ to the ROSA26 locus via homologous recombination (fig. S1). One clone, exhibiting (i) membrane-bound tdTomato signal, (ii) ES morphology (tight and dome-shaped colonies), and (iii) single-copy insertion in the ROSA26 locus as evidenced by Southern blotting, was selected (Fig. 1A and fig. S1, B to D). The transfection process and presence of the transgene had no significant effect on the pluripotency of the transgenic ESC line ($ChR2^{H134R}$-HBG3) relative to the parental line (HBG3), as demonstrated by immunostaining of Oct4 (Fig. 1A) and the RNA expression levels of five pluripotency markers (*Oct4*, *Nanog*, *Sox2*, *Esrrb*, and *Klf4*) (fig. S1E).

ESCs were then differentiated into MNs following a published protocol (*55*) consisting of the formation of embryoid bodies (EBs) and exposure to retinoic acid (RA) and smoothened agonist (SAG) (see Supplementary Materials and Methods). By day 6 of differentiation, MNs could be identified by their GFP expression while retaining a strong expression of tdTomato::$ChR2^{H134R}$ throughout the neurospheres (Fig. 1B). Fluorescence-activated cell sorting (FACS) data (green channel for Hb9 and red channel for ChR) showed that a large majority of $Hb9^{GFP+}$ neurons still expressed tdTomato::$ChR2^{H134R}$ (93.7 ± 7.9%; $n = 6$) (Fig. 1C), indicating that differentiation does not interfere with transgene expression. Both double-positive $ChR2^{H134R}$-HBG3–derived MNs ($ChR2^{H134R}$-HBG3-MN) and $Hb9^{GFP+}$ parental HBG3–derived MNs (HBG3-MN) extended neurites within minutes following plating and assumed similar neuronal morphologies, suggesting proper development of the $ChR2^{H134R}$-HBG3-MN with respect to their parental line. All $ChR2^{H134R}$-HBG3-MN retained $ChR2^{H134R}$ expression (Fig. 1D) over a period extending beyond 16 days after plating, indicating no signs of long-term silencing of the transgene. As expected, both cytosolic GFP and membrane-bound $ChR2^{H134R}$ were present throughout the entire cell (somata and neurites) (Fig. 1D).

The functionality of Channelrhodopsin in $ChR2^{H134R}$-HBG3-MN and its ability to evoke APs was validated by patch clamp. Whole-cell recording was performed on double-positive MNs on days 3, 10, and 16 after plating. Resting membrane potential, resistance, and capacitance measurements revealed no differences between HBG3-MN and $ChR2^{H134R}$-HBG3-MN (fig. S2A), suggesting no alteration of the basal electrical properties following ESC targeting, and are consistent with previous reports on HBG3-MN (*13*). Peak (I_P) and steady-state (I_{SS}) photocurrents of the $ChR2^{H134R}$-HBG3-MN during photostimulation were found to be −142 ± 30 pA and −84 ± 20 pA, respectively, on day 3, reaching −3.8 ± 1.9 nA and −385 ± 71 pA by day 10 and −4.7 ± 1.7 nA and −588 ± 230 pA by day 16 (Fig. 1, E and F), whereas the ChR-free parental HBG3-MN remained unresponsive to optical stimulation (Fig. 1E). As expected, elicited currents decreased with stimulation light intensity and with a shift of wavelength from blue to green excitation (fig. S2B). AP could be evoked in all cells from day 3 to day 16 (Fig. 1G). By day 10 onward, trains of AP could be elicited upon sustained illumination, consistent with natural neuronal maturation. Stimulation wavelength, irradiance, pulse frequency, and pulse width dependence on inward currents and AP elicitation were also characterized and yielded similar results as previously reported on optogenetically modified primary hippocampal or hES-derived neurons (fig. S2, B to F) (*48*, *56*). These results fully validate the ability to form optically excitable MNs from a photosensitized standard mESC line.

$ChR2^{H134R}$-HBG3–derived MNs can stimulate muscle contraction in adherent in vitro cultures

We next demonstrated the ability of the $ChR2^{H134R}$-HBG3-MN to form functional NMJs with C2C12-derived skeletal muscles. This in vitro demonstration of optically excitable NMJs was conducted using a traditional dish assay, consisting of dissociated MN plated on top of a layer of contractile myotubes, commonly used for MN-muscle cocultures (*13*, *17*). As early as 6 hours after plating, neurite outgrowth could be seen, and by day 1, the first contacts with muscle cells were observed (Fig. 2A). The first muscle contractions could be optically triggered by day 3, consistent with results reported with electrically stimulated NMJ in vitro (*17*). This phenomenon was monitored for another 3 days during which the light-driven muscle contraction persisted (Fig. 2, B and C, fig. S3A, and movie S1). This was further confirmed by the inhibition of light-induced muscle contraction in the

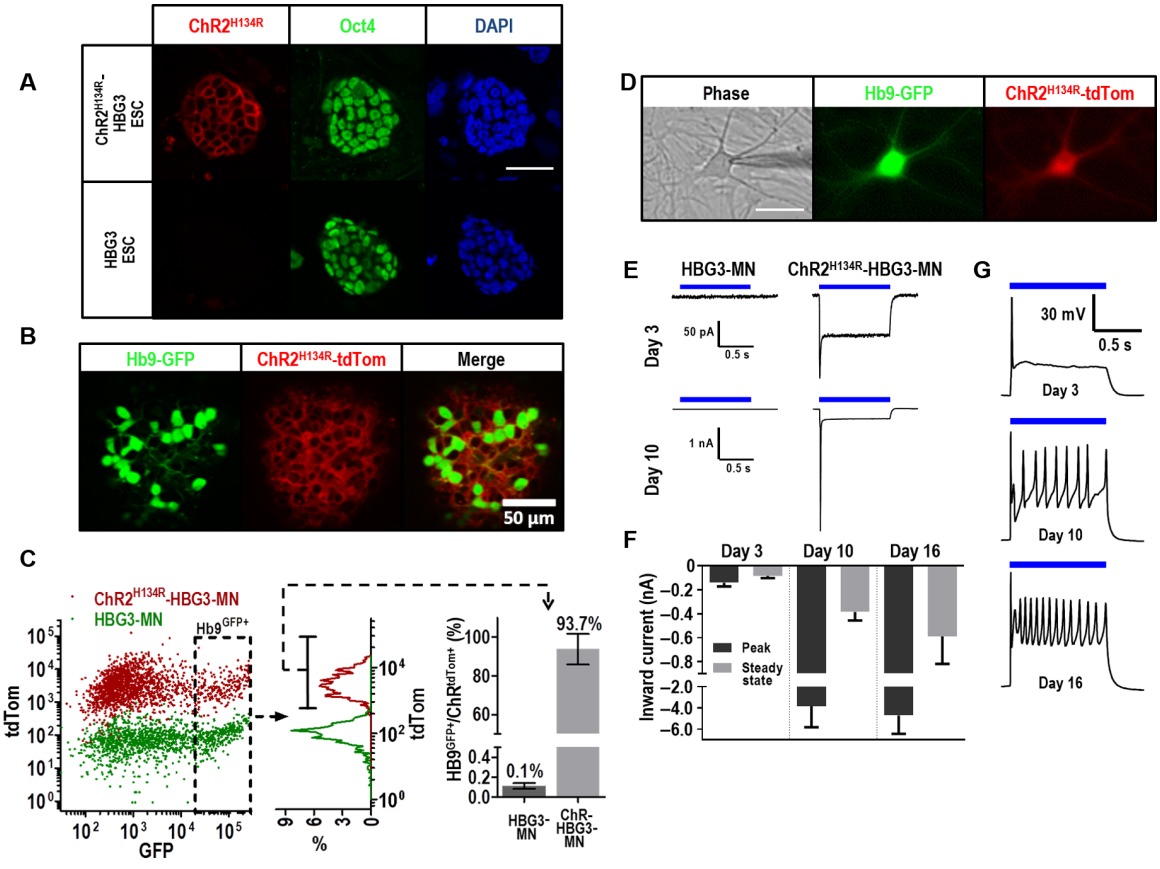

Fig. 1. ChR integration via homologous recombination results in stable expression in ESC and ES-derived MNs and proper light-driven neuronal stimulation. (**A**) Membrane-bound expression of tdTomato-tagged ChR2 is observed in transfected ES colonies. Immunostaining for Oct4 expression confirms the pluripotent nature of the transformed cells. Scale bar, 50 µm. DAPI, 4′,6-diamidino-2-phenylindole. (**B**) Confocal image of a ChR-HBG3–derived neurosphere on day 7 after RA and SAG treatment, showing persistent expression of ChR. (**C**) FACS data comparing tdTomato:: ChR expression of parental (HBG3-MN) and ChR-expressing (ChR-HBG3-MN) cells dissociated from day 7 neurospheres, demonstrating robust expression and minimum silencing after reaching the MN lineage. (**D**) Dissociated $Hb9^{GFP+}/ChR^{tdTom+}$ MN plated on a monolayer of cortical glial feeder cells assuming proper neuronal morphology on day 3. The phase contrast image features the patching electrode. Scale bar, 50 µm. (**E**) Representative trace displaying inward current upon optical stimulation (blue bar) on days 3 and 10 on HBG3-MN and ChR^{H134R}-HBG3-MN. (**F**) Peak and steady-state inward currents on days 3, 10, and 16 in ChR-HBG3-MN (n = 10). Error bars, SD. (**G**) Representative current-clamp recordings upon prolonged 1-s optical stimulation displaying AP elicitation on days 3, 10, and 16.

presence of α-bungarotoxin (αBTX), an AChR antagonist (17 of 17 myocytes, which was light-responsive before αBTX treatment, showed inhibition after treatment) (Fig. 2B). Moreover, the presence of spontaneous twitches after αBTX application was a confirmation that the treatment did not alter the contractility of the myocytes (fig. S3B).

To test the versatility and spatial selectivity of optogenetic stimulation of NMJ, we reduced the diameter of the excitation light beam to ~100 µm, delivering illumination to defined locations in the vicinity of the myotube. When optically exciting one neighboring cluster of MNs (Fig. 2C, i, region 3), no contraction was observed (Fig. 2C, ii, trace 2), a result similar to the one obtained by illuminating the muscle cell alone (Fig. 2C, i, region 2, and ii, trace 3), indicating that that particular cluster of neurons did not form functional NMJs with that myotube. However, when illuminating another neuron cluster (Fig. 2C, i, region 4), the muscle exhibited the same contraction pattern as when the whole field of view was uniformly stimulated (Fig. 2C, i, region 1, and ii, traces 1 and 4). This illustrates the selectivity of optogenetic stimulation and shows how localized optical excitation can help decipher connectivity patterns.

Design of the microfluidic device allows for 3D and compartmentalized coculture of MNs and muscle bundles

The new 3D platform developed in this study capitalizes on key advances featured in existing muscle and NMJ cultures in that it combines the coculture compartmentalization of MNs and myofibers, as found in 2D systems, the force sensing capability, and the 3D nature of the mechanically compliant matrix surrounding the cells. Neuromuscular tissues were created in a polydimethylsiloxane (PDMS)–based device consisting of two parts (Fig. 3). The top microfluidic section is patterned with three gel regions flanked with two medium channels (Fig. 3A). The left (receiving the neurospheres) and middle gel regions are both 0.5 mm in width, whereas the right 1-mm-wide channel will

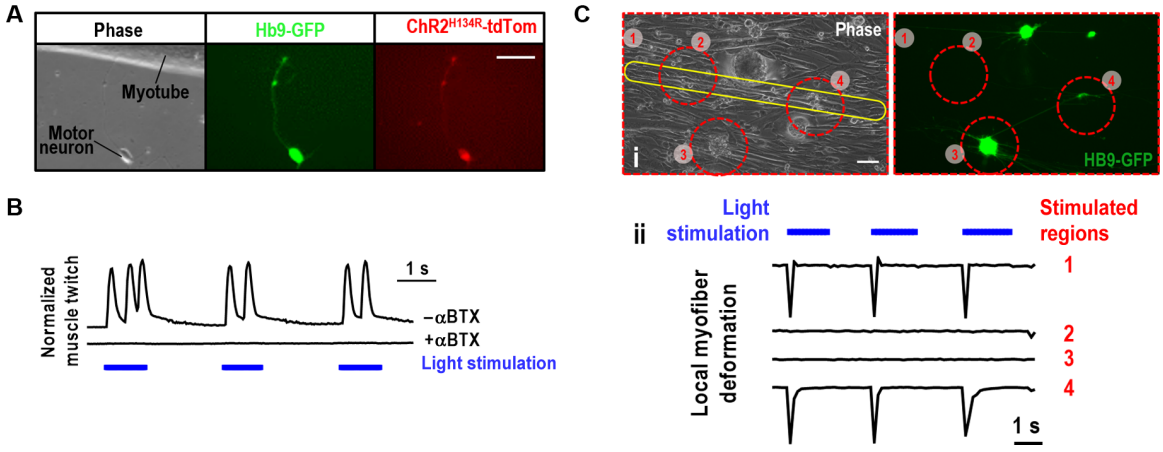

Fig. 2. ChR-HBG3-MN form functional NMJs in vitro in adherent cultures. (**A**) Dissociated Hb9^{GFP+}/ChR^{tdTom+} MN forming initial contact with a C2C12-derived myotube after 1 day of coculture. Scale bar, 50 μm. (**B**) Muscle contraction observed upon optical stimulation (blue bar) of the ChR-HBG3-MN. The contractions were inhibited after incubation with αBTX. (**C**) Local optogenetic excitation of neuron-muscle coculture: (i) phase contrast and epifluorescence images of ChR-HBG3-MN and muscle cells. The myotube of interest is outlined in yellow, and the stimulated regions are outlined by the red dashed line. Scale bar, 100 μm. (ii) Muscle twitch [outlined in yellow in (i)] as light stimulation (blue bars) is applied to various regions outlined in red: full field of view (1), muscle only (2), noninnervating MN cluster (3), and innervating cluster (4).

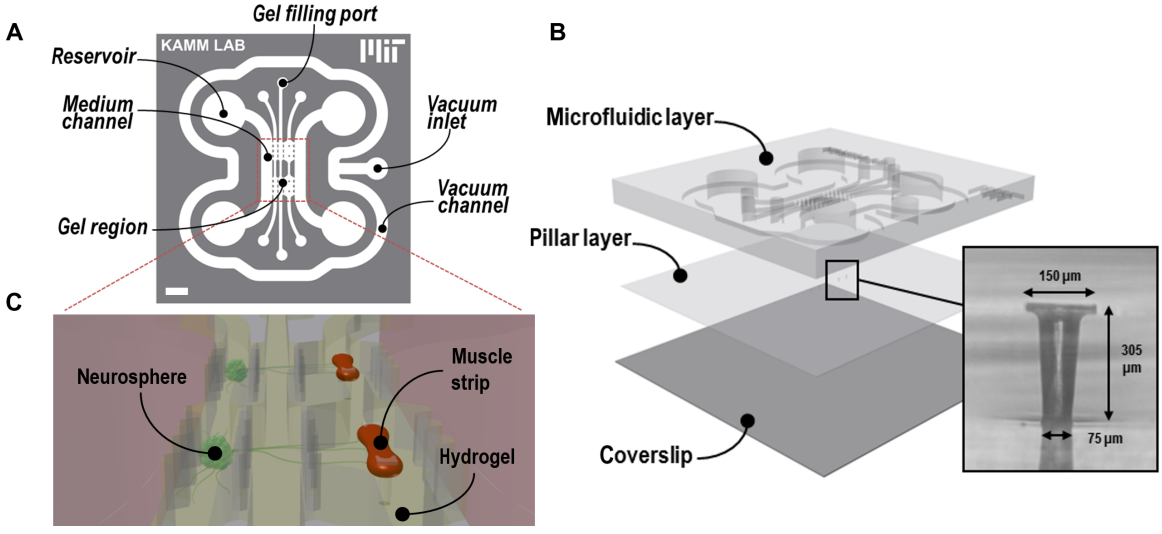

Fig. 3. Microfluidic design and assembly. (**A**) The microfluidic design features three parallel gel regions accessible by six gel filling ports and flanked by two medium channels connected to four medium reservoirs. A surrounding vacuum channel allows for temporary bonding. Scale bar, 2 mm. (**B**) The platform is composed of a top microfluidic layer assembled on top of a PDMS membrane featuring two sets of two capped pillars (inset), itself bonded to a coverslip. (**C**) Schematic displaying the final coculture arrangement: embedded in a hydrogel, muscle bundles that are wrapped around and exerted force to the pillars are innervated by neurospheres located in the opposite gel chamber separated by a 1-mm-wide gel region.

receive the muscle strip (Fig. 3, A and C). Each channel is separated from its neighbors by a row of posts, which provide confinement during gel and cell seeding while still allowing cell-cell signaling and nutrient supply. The height of the channels is 320 μm throughout the device, allowing for the tissue to experience a full 3D environment. A necking of the gel region allows for the formation of two independent and isolated tissues, each ~1 mm long (Fig. 3A), doubling the throughput of the platform. The bottom section of the platform is a thin membrane of PDMS (~100 μm), bonded to a coverslip for rigidity, featuring two sets of two capped pillars (Fig. 3B). The 15-μm difference between the top of the pillar and the roof of the channel allows for pillar deflection. Following proper sterilization, the platform is assembled by affixing the top section to the bottom one such that the pillars line up in the center of the muscle channels (Fig. 3, A and C) (see Supplementary Materials and Methods). This design is unique in its ability to culture MNs and muscle cells in a 3D environment while keeping them physically separated. This

facilitates the monitoring of axonal outgrowth in a functional context, and potentially providing cell-specific factors or drugs.

The following stepwise seeding procedure was optimized to account for the myoblast-induced compaction of the hydrogel occurring within hours of C2C12-laden matrix seeding, which prevents simultaneous coseeding and in situ codifferentiation of both cell types (Fig. 4). First, C2C12 cells, suspended in a collagen-Matrigel solution, were seeded into the rightmost channel of the device containing the pillars (Figs. 3C and 4, day 0). Following gel compaction (Fig. 4, day 1, and movie S2), resulting in gel fiber rearrangement and myoblast alignment (*35*, *57*), thin pieces of tissue remained, connecting the muscle strips together and to the gel filling ports and preventing them from contracting independently from each other. To allow pillar deflection upon muscle contraction, the separation and mechanical decoupling of the muscle strips was accomplished by a manual ablation. Another technique involving two-photon laser excitation was also developed and is described in more detail in Supplementary Materials and Methods. After removing the reversibly bonded top layer of the device, a needle was used to perform incisions to the muscle strips at a distance of ~500 μm from the pillar (Fig. 4, day 2). The total resorption of the small "tails" left by the ablation was completed over the following day, resulting in well-delineated muscle bundles (fig. S4, B and C). After ablation, differentiation was induced by switching to a myogenic differentiation medium. The expression of α-actinin and the formation of striated sarcomeric structures, indicative of proper differentiation, were visualized by immunostaining and confocal imaging (Fig. 5A and fig. S5D). The muscle bundle exhibited an initial 75% compaction following seeding, reaching ~85% on day 6, and its width finally stabilized to 25% of the original dimension (Fig. 5B)

To monitor contractile activity and functionally assess myogenic differentiation, we optogenetically modified C2C12 cells and optically stimulated the muscle strips derived from these cells (fig. S5) [the C2C12 photosensitization was performed similarly to previous studies (*57*, *58*); see Supplementary Materials and Methods]. Light-induced contractions were initially observed on day 3 after induction. Throughout the entire process, passive tension (F_P) and active contraction (F_A) were measured by monitoring pillar deflection (see Supplementary Materials and Methods). Both were comparable to those measured in previous in vitro platforms (*33*, *57*), with passive tension reaching a plateau after day 7 at ~18 μN and tetanus occurring at 10 Hz (Fig. 5C and fig. S5C). Overall, there was no evidence to suggest that confinement of the myoblasts to a microfluidic chamber altered myogenesis.

Neuron-muscle cocultures in the microfluidic devices were initiated by seeding the ChR2^{H134R}-HBG3–derived neurospheres into the device after 7 days of differentiation (Fig. 4, day 7). After reassembling an

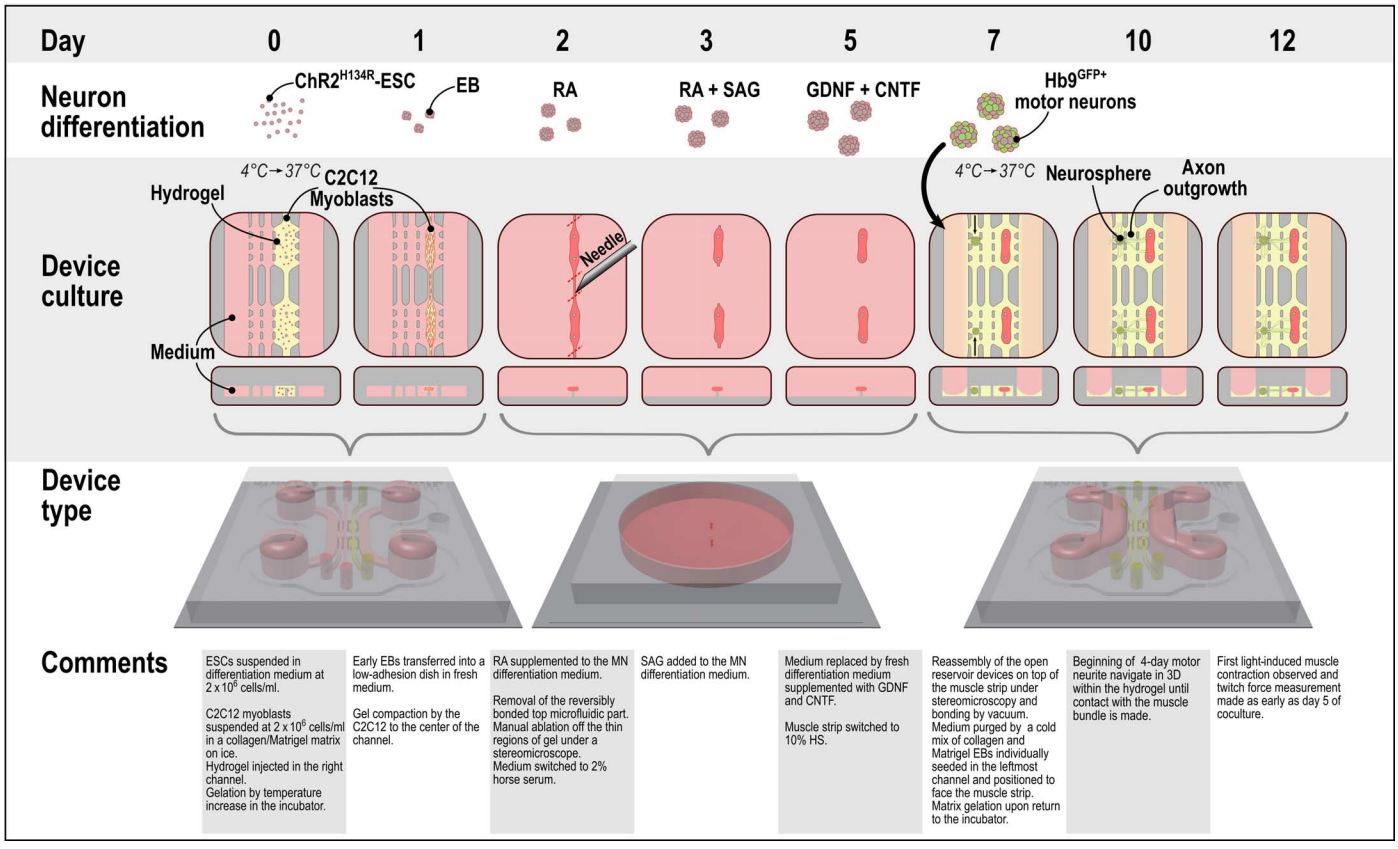

Fig. 4. Framework for the microfluidic neuromuscular coculture. (**Row 1**) Schematic showing the differentiation process of the ESCs into MNs following a previously published protocol (*37*). (**Row 2**) Schematics displaying the top and front views of the tissue in the microfluidic platform. (**Row 3**) 3D computer-aided drafting illustrations showing the version of the platform used at the corresponding days. CNTF, ciliary neurotrophic factor; HS, horse serum.

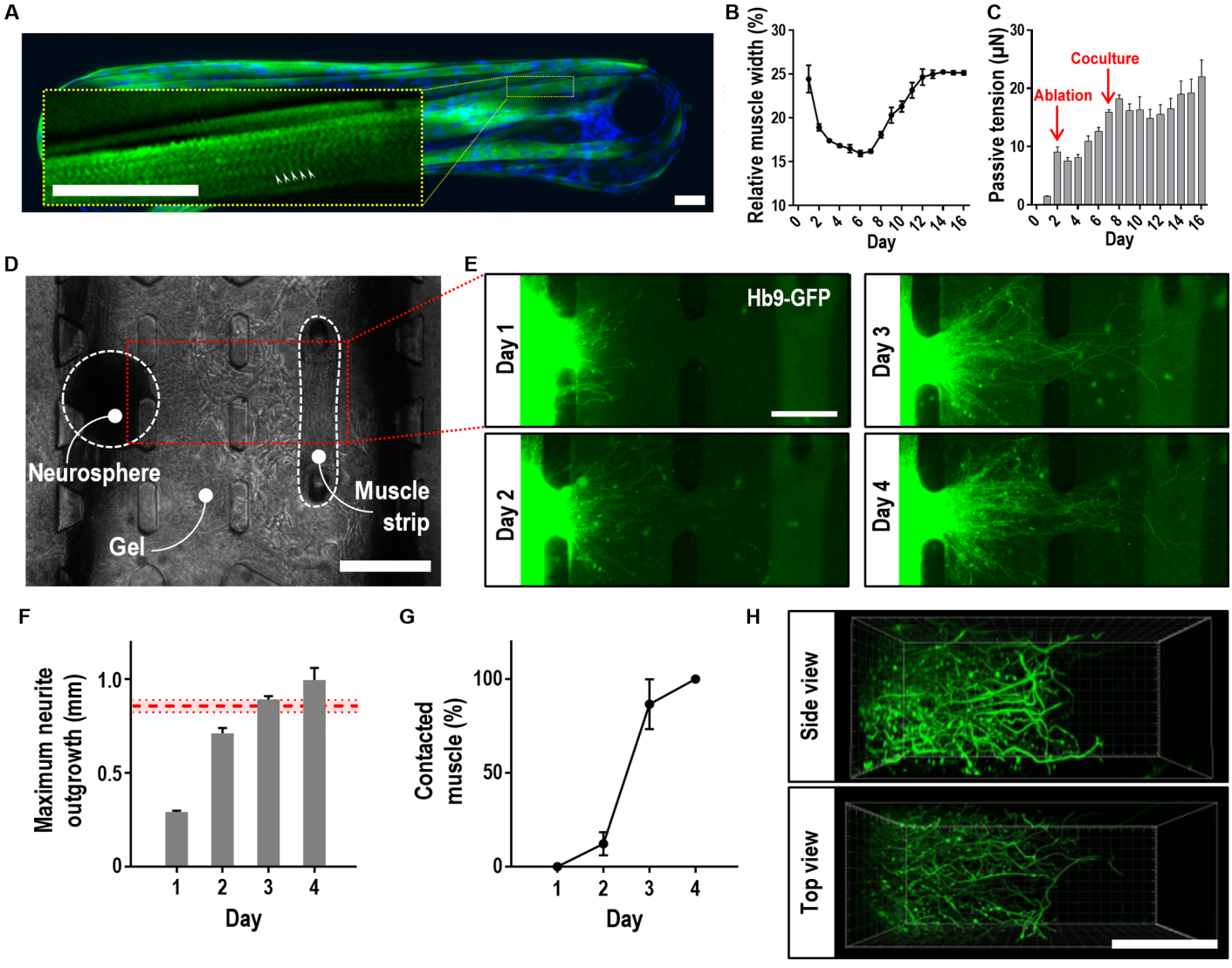

Fig. 5. Muscle differentiation and neuromuscular tissue formation. (**A**) Immunostaining of the myogenic marker α-actinin (green) and DAPI (blue), demonstrating proper muscle differentiation and formation of sarcomeric striations (examples of striations are indicated by arrowheads in the inset). Scale bars, 50 μm. (**B**) Muscle bundle width relative to the width at day 0. (**C**) Passive force generation over the course of 16 days. (**D**) Representative image of a neuron-muscle coculture in the microfluidic device on day 1 of coculture. Scale bar, 500 μm. (**E**) Neurite extension over 4 days of coculture. Scale bar, 250 μm. (**F**) Absolute maximum neurite outgrowth in millimeters over the first 4 days of culture. For comparison, the red dashed line represents the average initial distance between neurospheres and muscle bundles (the shaded area in between the dotted line indicates the SEM). (**G**) Percentage of muscle bundles contacted by at least one neurite over the course of 4 days. (**H**) Confocal 3D reconstruction of neurites in the bridge gel region after 1 day of coculture. Scale bar, 200 μm. All error bars, SEM.

open-reservoir variant of the microfluidic device onto the muscle strip under a stereomicroscope, the medium was aspirated from the reservoirs, and the one contained in all channels was flushed with a collagen-Matrigel mix prepared on ice (see Materials and Methods). Neurospheres ~300 to 400 μm in diameter were manually selected, resuspended with the same chilled collagen-Matrigel mixture as above, and individually pipetted into the leftmost channel (Figs. 4 and 5D) before the devices were placed in the incubator for matrix gelation, after which medium was supplied to both open reservoirs. The diameter of the neurospheres being greater than the interpost distance ensured their restriction to the assigned channel, resulting in a physical separation of ~1 mm between the neurons and the muscles.

Because this platform was the first to create a matrix-embedded muscle strip anchored to compliant pillars, as opposed to the existing stand-alone ones suspended in medium (*44*, *45*), we characterized the effect of the presence of the gel on the force exerted by the muscle on the pillars. This was achieved by measuring the force applied to the pillars before and after gel seeding (on the basis of the assumption that the

force generated by the muscle is not altered during the ~20-min polymerization process). Considering the poroelastic properties of hydrogel, we anticipated that its mechanical contribution would bias the force measurement (fig. S6A). However, results revealed no significant changes in the peak or steady-state force, along with the rate of force increase (fig. S6, B and C), suggesting that the contributions of the viscoelastic/poroelastic properties of the gel were negligible. Therefore, the force generated by the muscle strip can be determined from pillar deflection without correcting for matrix viscoelasticity.

One day after seeding, motor neurites could be seen extending from the neurospheres, as evidenced by the presence of $Hb9^{GFP+}$ processes in the gel (Fig. 5, D and E). All $Hb9^{GFP+}$ neurites were also positive for $ChR2^{H134R}$, confirming once more minimal silencing of the transgene. Some $Hb9^{GFP-}/ChR^{tdTom+}$ neurites were also observed (fig. S7A), indicative of the presence of non-MN cells, most likely interneurons as previously reported in HBG3 ESCs differentiated under similar conditions (*59*). Maximum axon outgrowth rate was measured to be $10.4 \pm 5.6\ \mu m\ h^{-1}$ over the course of the first 4 days [consistent with the axon 3D outgrowth reported in the literature (*19*, *60*)], after which all muscle strips were contacted by motor axons (Fig. 5, E to G). Interestingly, the direction and rate of outgrowth were not found to be biased by the presence of the muscle strip (fig. S7B). The spatial segregation of the two cell types provides a unique opportunity to visualize the 3D axon outgrowth toward the muscle. Confocal imaging was used to assess the distribution of extended neurites within the thickness of the gel at different stages of the coculture within the central channel (Fig. 5H and movie S3). Images reveal that no plane was preferred for neurite outgrowth as they extended homogeneously throughout the gel.

$ChR2^{H134R}$-HBG3–derived MNs remotely innervate myofibers and activate muscle contraction upon illumination in the 3D microfluidic device

Glutamate, the natural excitatory neurotransmitter for lower MNs and commonly used to demonstrate the presence of functional NMJs, was added to the medium at a concentration of 400 μM and introduced to the leftmost channel of the device, adjacent to the gel region that houses the neurospheres. The first muscle contraction, indicative of the presence of functional NMJs, was recorded 80 s after glutamate administration, and the twitching frequency rose during the subsequent 120 s to reach a steady value of ~1.25 Hz (Fig. 6A). The delay in contraction and increase of the twitching frequency are likely due to the diffusion of the glutamate to the MNs embedded in the ECM because this lag is absent in adherent 2D cultures (*61*) or 3D constructs in suspension (*35*).

The use of our $ChR2^{H134R}$-HBG3-MN enabled faster and more controllable muscle stimulation. Light-driven muscle contraction could be recorded 5 days following neurosphere seeding (day 12), with no discernable patterns in amplitude or frequency, and persisted until the end of the 16-day experiment period, demonstrating the robust nature of the NMJs in this device (Fig. 6B and movie S4). Contractile forces measured by the compliant pillars were on the order of ~1.5 μN, comparable to those obtained by glutamate stimulation. Similar to the 2D case, the application of αBTX inhibited muscle contraction, confirming the functionality of NMJs in the 3D device (Fig. 6B). Moreover, we observed that the distal part of motor axons colocalized with αBTX-stained AChR, a visual assessment of the presence of NMJs (Fig. 6C). Sustained light illumination was found to generate multiple muscle twitches (Fig. 6, B and D), with frequency increasing as the stimulation light intensity increased (Fig. 6, D and E), consistent with the patterns of trains of AP generated under the same stimulation conditions (Fig. 1). However, no muscle tetanus could be generated. We found that the maximum force generated via neuronal stimulation (chemical or optical) yielded forces 70% that of the maximum force that could be generated via electrical excitation or by optically stimulating $ChR2^{H134R}$-expressing C2C12-derived muscle bundles, suggesting an incomplete innervation of the whole muscle strips by the same factor (assuming that all myofibers can generate similar levels of contraction).

DISCUSSION

The combination of microfluidic and optogenetic technologies has enabled the development of a highly controllable and physiologically relevant in vitro model for motor units, with applications ranging from fundamental scientific studies to drug screening assays. Light stimulation of ChR-expressing ES-derived MNs provides great versatility over the excitation of the tissue by making it cell-specific and more spatiotemporally resolved than chemical stimulation. The PDMS-based microfluidic platform encompasses technologies that bring together essential aspects of neuromuscular tissue culture, namely, the 3D compartmentalized nature of the neuron-muscle coculture along with a functional force readout.

The microfluidic chambers provide a 3D configuration similar to that of the native tissue, where one channel serves as a surrogate for the spinal cord, whereas the other one models the remotely innervated muscle tissue as found in the body wall or limbs. This culture system confers not only a softer mechanical substrate that 2D systems often lack but also the ability to investigate the role of the surrounding ECM. Compartmentalization further facilitates visualization of axonal outgrowth and innervation through a relevant matrix or the supply of cell-specific chemical cues and would allow for the manipulation of axons without interfering with other cell types. Finally, the integration of force sensors to the design offers a live, noninvasive, and quantitative assessment of muscle differentiation and contraction and synapse function.

First, the ability to photosensitize nonaltered ESCs and differentiate them into optically excitable MNs raises the potential for more versatile ways of investigating disease models, such as SMA or ALS, by delivering ChR to the commercially available patient-derived iPS cells, already shown to be differentiable into functional MNs (*62*, *63*). This is a process that could be combined with recent advances in transcriptional programming that drastically increase the yield and decrease the duration of MN differentiation from human ESC and mESC (*64*, *65*). The demonstration of optically controlled NMJs in vitro will find application in diverse fields. For instance, much is yet to be understood regarding the process of NMJ maturation and remodeling, specifically how activity or exercise is responsible for plastic synaptic adaptation (*24*). The ability to selectively excite MNs or muscle cells [by selectively expressing ChR in one or the other or taking advantage of wavelength-specific opsin variants (*66*)] will greatly facilitate identifying the contributions of each synaptic partner in their anterograde and retrograde signaling (*67*–*69*). We also foresee applications in the fields of soft robotics or nanorobotics, defined as microfabricated motile substrates actuated by muscle cells recapitulating locomotive tasks (*70*–*74*). The use of optogenetic MNs will provide a level of spatiotemporal control capable of emulating the fine input command of the motor cortex.

Overcoming the challenges of coculturing optogenetically modified MNs and skeletal muscle cells in a microfluidic device, featuring a compliant 3D matrix and in a spatially organized and compartmentalized fashion, all contributed to creating an NMJ microenvironment that brings together fundamental aspects of physiological neuromuscular tissues. The confinement by a microfluidic chamber did not impair myogenesis, and neither did the presence of the surrounding hydrogel. The spontaneous axonal outgrowth allowed for a remote innervation and emergence of light-excitable NMJs. Although the isotropic neurite outgrowth could be the result of a weak chemotactic gradient generated by the muscle-derived factors, another explanation is that the MNs are not mature enough to express the appropriate chemoattractant receptor or that the subtype of MNs thus differentiated is irresponsive to the factors secreted by the muscle cell (*75*–*77*). The ability to isolate the motor somata from the muscle cells is crucial for imaging the navigation of axons within a wide extracellular space and could prove useful in further understanding the process of nerve degeneration and repair in a functional context. Moreover, with some further engineering of the muscle consisting of fluorescently tagging the AChRs (*78*) or postsynaptic scaffolding proteins, such as Rapsyn (*79*), one could monitor the time course of synapse remodeling upon MN or muscle stimulation (*69*). This feature is also the first of its kind to allow for the supply of each cell type with its own medium in such a 3D environment in the form of two opposite gradients [as demonstrated with fluorescent tracers (fig. S8)]. This medium segregation could enhance neuromuscular tissue survival and NMJ maturation in vitro, which could be beneficial for long-term NMJ cultures (*80*). In addition, this asymmetry of chemokine supply can be used in a variety of applications, from testing the influence of cytokine gradients in the context of spinal cord development and axon pathfinding to the supply of cell-specific drugs.

Although contact between motor neurites and muscle bundles was observed by day 4 of coculture in all tissues, only ~50% of the muscle constructs could be stimulated via neuronal excitation. This moderate success rate in generating functional light-excitable NMJs and incomplete innervation is likely attributable to poor accessibility of the myofibers to the incoming growth cone, because some were found within the muscle bundle. A potential solution to this problem could be

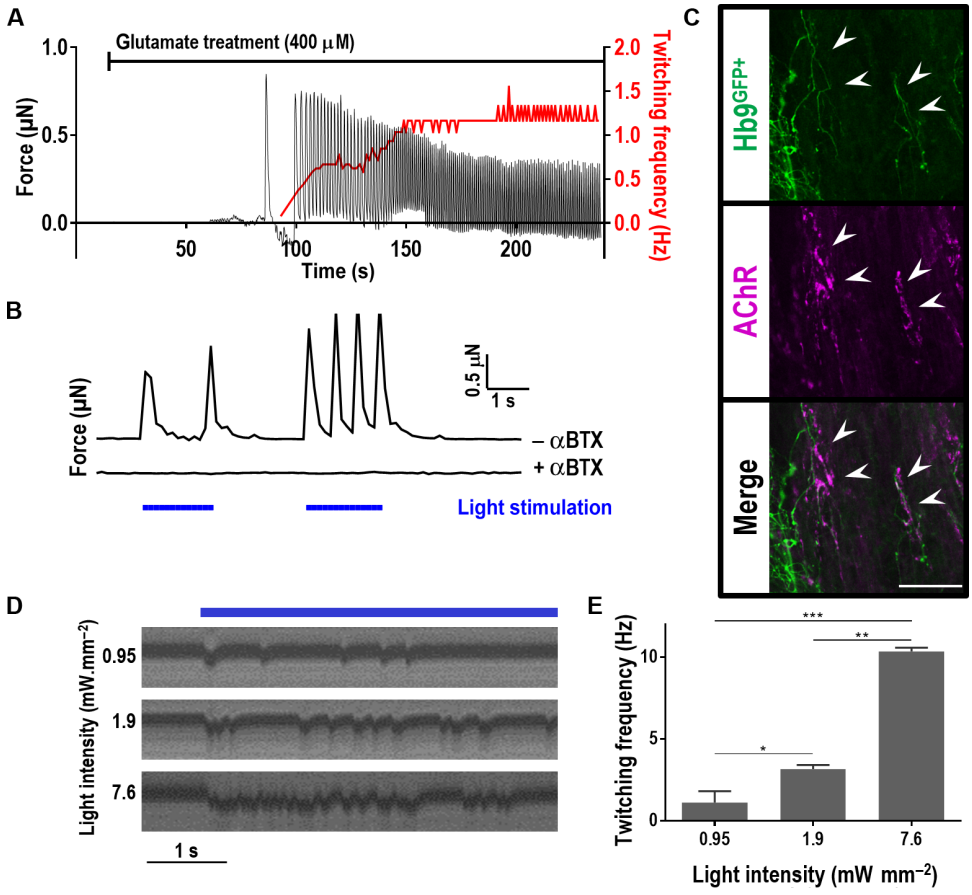

Fig. 6. Activation of NMJs within the microfluidic device. (**A**) Application of glutamate to the medium results in a delayed stimulation of the muscle, leading to the initiation of muscle twitching with force (left *y* axis) at an increasing frequency (right *y* axis) as glutamate diffuses within the neurospheres. (**B**) Force generated by the muscle bundle upon illumination of the ChR2^{H134R}-HBG3-MN neurospheres on day 15. Application of αBTX inhibited the contractions. (**C**) Colocalization of incoming motor axons and clusters of AChR indicative of the presence of NMJ. Scale bar, 100 μm. (**D**) Kymographs of the pillar displacement on day 16 for three stimulation light intensities. (**E**) Muscle-twitching frequencies as a function of light intensity. *P < 0.05, **P < 0.001, ***P < 0.0005.

to form multiple thinner muscle strips as described recently, which would provide more entry points to incoming axons (*81*, *82*). Moreover, the resulting force that was 70% of the maximum force generated by total myofiber recruitment could find an extra explanation in the fact that tetanus could not be observed in muscle bundles stimulated by the MNs (whereas they were via direct electrical excitation). Although consistent with the existing studies conducted on NMJ formed in vitro with either C2C12 or primary myoblasts (*15*, *30*, *35*, *40*), these systems could benefit from both recent myogenesis protocols from heterogeneous primary muscle cultures resulting in physiologic force generation (*83*), and genetically modified GDNF-expressing ESC-derived MNs leading to higher survival and firing rate (*53*).

To further increase the physiological relevance of the system, other cell types could be added to the culture. This could be done either by taking advantage of, or even tuning, the heterogeneity of the differentiated cells within the neurospheres (the non-MN ChR2-expressing cells in fig. S7A are likely to be interneurons interacting via excitatory or inhibitory signals) or by complementing the surrounding matrix with supporting cells. For instance, Schwann cells, responsible for axon guidance, myelination, nerve repair (*84*), or NMJ formation and function (*5*, *10*), could be added to the surrounding hydrogel. Doing so could also provide precious functional and quantitative insight in the myelination process along with demyelinating neuropathies, such as the Guillain-Barre syndrome (*85*) or Charcot-Marie-Tooth disease (*86*).

The integration of compliant micropillars as anchoring points for the muscle bundles allows for a rapid, passive, and noninvasive assessment of muscle passive tension and active contraction. In a drug-screening assay, this contractile functional output provides a means of assessing the downstream and cumulative efficacy of a drug on motor unit recovery, a method used in the past in muscle bundle cultures (*87*) or in NMJ culture on cantilevers (*40*) and termed high-content screening. Ongoing work is focusing on increasing the throughput of the system to make this possible and would provide a new addition to the ever-growing list of organs on a chip (*88*).

MATERIALS AND METHODS

Microfluidic device fabrication

The mold fabrication followed a process similar to previously reported (*41*, *42*). Briefly, designs were generated using AutoCAD (Autodesk), and the patterns were transferred to a Mylar transparency mask using high-resolution printing (FineLine Imaging). Silicon wafers were then fabricated by photolithography using an SU-8 photoresist (MicroChem). Unlike the top microfluidic part of the device that was casting from a negative mold, the master for the bottom pillar part was a positive version of it. All molds were surface-treated overnight before any PDMS (Ellsworth Adhesives) casting using (tridecafluoro-1,1,2,2-tetrahydrooctyl)-1-trichlorosilane (United Chemical Technologies). For the top microfluidic part, PDMS, mixed at 10:1 base/curing agent, was poured onto the silicon mold at a height of 5 mm, degassed in a desiccator, and cured at 80°C for at least 4 hours. Devices were then cut off the mold and trimmed to the appropriate size, and gel filling ports, vacuum port, and medium ports/reservoirs were formed with 1-, 2-, and 4-mm-diameter biopsy punches, respectively. For the bottom pillar part, a negative version of the mold was made with PDMS mixed at a 5:1 base/curing agent. It was then silanized overnight, and the same PDMS mixture was spun on top of the negative mold for 10 s at 500 rpm and 15 s at 1000 rpm, yielding membranes with thicknesses of ~100 μm. The membrane featuring the pillars was gently peeled off. Each pillar had a slight conical shape, reminiscent of the microfabrication process, with basal and tip diameters of 75 and 100 μm, respectively, and a height of 280 μm. The membrane pillar devices were then bonded to a 20-mm × 20-mm coverslip by plasma activation (Harrick Plasma) for rigidity purposes. The caps of the pillars consisted of 150-μm × 150-μm squares of 25-μm-thin PDMS (obtained by spin-coating it on a 10-cm Petri dish lid for 30 s at 5000 rpm), manually positioned over the pillar, and glued with uncured PDMS, which resulted in a total height of 305 μm. Both top and bottom parts of the device were then cleaned by sonication in a bath of ethanol, followed by a sonicated bath of deionized (DI) water. They were then sterilized by a cycle of wet autoclaving, followed by dry autoclaving. The parts were aligned and assembled using a stereomicroscope under sterile conditions. After usage, the devices were cleaned by sonication in ethanol and then DI water, sterilized by autoclaving (a wet cycle followed by a dry cycle), and stored in a sterile container before further use. No devices were used more than 10 times.

Cell culture and differentiation

Source cells. mESC line HBG3 (Hb9-GFP), a gift from H. Wichterle, Columbia University, NY, was kept in culture on a feeder layer of mouse embryonic fibroblasts (CF-1 MEF Feeder Cells, Applied StemCell) plated on 0.1% gelatin–coated dishes in undifferentiated medium consisting of EmbryoMax ES Dulbecco's modified Eagle's medium (DMEM) (Millipore Chemicon), 15% ESC-qualified fetal bovine serum (Invitrogen), 1% nucleosides (Millipore Chemicon), 1% nonessential amino acids (Millipore Chemicon), 1% penicillin-streptomycin (Invitrogen), 1% L-glutamine (Invitrogen), 0.1 mM β-mercaptoethanol (Sigma), and 0.1% leukemia inhibitory factor (EMD). Mouse myoblasts C2C12 (*89*) [American Type Culture Collection (ATCC)] were cultured below 70% confluency in growth medium consisting of high-glucose DMEM (ATCC), 10% fetal bovine serum (Invitrogen), and 1% penicillin-streptomycin. All cells were kept in incubators at 37°C and 5% CO_2. None of the cells were used beyond a passage number 20.

Motor neurons. The MN differentiation protocol was adapted from published literature (*55*). Briefly, mESCs were collected from their feeder layer culture and plated at 2×10^6 cells in 10 ml in a 10-cm Nunc culture dish in differentiation medium, consisting of 1:1 Advanced DMEM/F-12 (Invitrogen)/Neurobasal (Invitrogen), 10% KnockOut Serum Replacement (Invitrogen), 1% penicillin-streptomycin (Invitrogen), 1% L-glutamine (Invitrogen), and 0.1 mM β-mercaptoethanol (Sigma). They were allowed to form EBs overnight. The next day, EBs in suspension were collected and transferred to low-adhesion culture dishes in 10 ml of differentiation; the cells that had attached to the Nunc dishes were discarded. On day 2, the medium was changed and supplemented with 1 μM RA (Sigma) and, on day 3, with 1 μM SAG (EMD). The cells remained in this medium for two more days. On day 5, the medium was replaced by differentiation medium supplemented with GDNF (10 ng ml^{-1}) (R&D Systems) and CNTF (10 ng ml^{-1}) (R&D Systems). EBs were used on day 7, either seeded in the microfluidic devices or dissociated and FACS-sorted to isolate $Hb9^{GFP+}$/ChR^{tdTom+} MNs for plating on a glial feeder layer or muscle cell in 2D cultures.

MN–glial cell coculture for electrophysiological recordings. Petri dishes (35 mm, BD Biosciences) were coated with a poly-D-lysine

(PDL) (Sigma) coating solution at a concentration of 200 μg ml^{-1} and incubated at 37°C overnight. After PDL solution was washed with DI water, a laminin coating solution (Invitrogen) was used at a concentration of 10 μg ml^{-1} and incubated for at least 4 hours. The laminin coating solution was rinsed once before glial cells (Supplementary Materials) were plated at ~1×10^5 cells per dish and allowed to form a monolayer over at least 5 days in high-glucose DMEM (ATCC) containing 10% HS (Invitrogen) and 1% penicillin-streptomycin (Invitrogen). Dissociated MNs were then plated at 1×10^5 cells per dish, and the medium was switched to MN growth medium supplemented with GDNF at 10 ng ml^{-1}, CNTF at 10 ng ml^{-1}, 3-isobutyl-1-methylxanthine (IBMX) (Sigma) at 100 μM, and forskolin (Sigma) at 10 μM. Half of the medium was replaced every day until the cultures were used for electrophysiological recordings.

MN–muscle cell coculture for NMJ in 2D. This procedure is a modified version of a previously published one (*17*). Similar to the glial cell culture, 35-mm Petri dishes were coated with PDL (200 μg ml^{-1}) and laminin (10 μg ml^{-1}). C2C12 cells were plated at ~1×10^4 cells cm^{-2} and cultured in growth medium. The next day, the medium was switched to high-glucose DMEM supplemented with 2% HS and 1% penicillin-streptomycin. Two days later, the medium was supplemented with cytosine arabinoside (AraC) (Sigma-Aldrich) (1 μg ml^{-1}) to eliminate the nonfused myoblast, and another 2 days later, early myotubes were trypsinized, replated at a 1:2 ratio on PDL- and laminin-coated 35-mm dishes, and cultured in medium consisting of 1:1 10% HS myogenic medium and neuronal differentiation medium supplemented with AraC (1 μg ml^{-1}). On day 4 after myogenic induction, dissociated and purified $Hb9^{GFP+}$/ChR^{tdTom+} MNs (see MN–glial cell coculture) were plated at 2×10^5 cells per dish. AraC was withdrawn from the medium and replaced with GDNF (5 ng ml^{-1}), CNTF (5 ng ml^{-1}), forskolin (5 μM), and IBMX (50 μM). In the subsequent days, half of the medium was replaced.

Cell seeding and differentiation in the microfluidic device

Cell seeding in the microfluidic device. All 3D cell cultures in the microfluidic devices were carried out in a collagen/Matrigel hydrogel in a 4:1 ratio. Rat tail type I collagen (Corning) was mixed on ice with 10× phosphate-buffered saline with phenol red (serving as a pH indicator), 0.5 N NaOH, and water for cell culture (Lonza) to yield a collagen concentration of 2 mg ml^{-1} at a pH of 7.4. Matrigel without growth factors (BD Biosciences) was thoroughly mixed with the collagen at 20% of the final gel mixture volume. The gel was then used within a few minutes following its preparation to avoid pre-polymerization.

C2C12 cells were trypsinized, counted, and centrifuged for 5 min at 200 rcf. The pellet was then resuspended in the hydrogel at a final density of 2×10^6 cells ml^{-1}. Shortly after resuspension, the hydrogel was injected into the rightmost channel of the microfluidic device that had been filled with medium before cell seeding. This later facilitated gel compaction because it allowed for the formation of a thin layer of medium that isolated the gel and the cells from the PDMS walls and reduced adhesion. The device was then placed in a humidified box and incubated at 37°C. To prevent cells from settling at the bottom of the device and ensuring a homogeneous distribution throughout the thickness of the channels, the devices were first placed upside down for 4 min and then rotated back to complete polymerization for the remaining 11 min. Growth medium was then supplied to the adjacent medium channel by forming a seal between a large-orifice pipette tip and the medium filling port and by pushing the medium into the channel. In the following days, the medium would seep through the dry channels to the left of the muscle chamber and fully wet all channels. The medium was replaced by removing approximately 50 μl of the old medium and replacing it with the same amount of fresh one. To prevent cross-flow that could wash off the gel, the medium was aspirated and supplied with a multichannel pipettor. The medium was changed every 24 hours.

Muscle differentiation. After tissue ablation (see Supplementary Materials and Methods), the muscle bundles were supplied with myogenic medium consisting of 2% HS DMEM (Fig. 4). Three days after induction, the medium was replaced by 10% HS myogenic medium (more adequate for the metabolically active muscle strips) until device reassembly and MN seeding.

Plasmid design and delivery

DNA constructs were created using standard molecular biology techniques. Briefly, a ChR2[H134R]-tdTomato expression cassette was cloned into the Ai9 ROSA26 targeting vector and linearized for mESC knock-in (fig. S1A). Ai9 was a gift from H. Zeng (Addgene, plasmid no. 22799). For lentiviral infection of C2C12 cells, ChR2[H134R]-tdTomato was cloned downstream of an elongation factor 1α (EF1α) promoter in a lentiviral plasmid (fig. S5A).

Mouse embryonic stem cell. The linearized ChR2[H134R]-tdTomato Rosa26 targeting vector (0.4 μg) was delivered to the mESC by nucleofection (Amaxa Nucleofector) for homologous recombination at the ROSA26 locus. Three days after plasmid delivery, a total of nine colonies were manually selected, on the basis of their ES-like morphologies and tdTomato expression, expanded, and tested for specific integration by Southern blotting. One clone displaying specific integration at the ROSA26 locus was selected for the rest of the study (fig. S1).

C2C12. For lentivirus production, HEK293FT cells were seeded into a T225 flask at 40% confluency 24 hours before transfection. Cells were transfected with 10 μg of EF1α-ChR2[H134R]-tdTomato, 10 μg of pMD2.G, 15 μg of psPAX2, 100 μl of Lipofectamine 2000 (Life Technologies), and 200 μl of PLUS Reagent (Life Technologies). Six hours after transfection, fresh medium was applied. Three days after transfection, virus supernatant was harvested, filtered through a 0.45-μm polyvinylidene difluoride filter (Millipore), aliquoted, and stored at −80°C. Lentiviral packaging plasmids (psPAX2 and pMD2.G) were a gift from D. Trono (Addgene, plasmid nos. 12260 and 12259). C2C12 cells were incubated with viral supernatant for 24 hours. The cells were cultured for 3 days, then expanded for another 3 days, and sorted by FACS. Fifty percent of the brightest cells were collected of the 12% of positive cells to tdTomato.

RNA extraction and reverse transcription quantitative polymerase chain reaction for gene expression analyses

RNA was extracted using Izol (5 PRIME, 2302700) according to the manufacturer's instructions. The extracted RNA (5 μg) was reverse-transcribed using M-MLV Reverse Transcriptase (Life Technologies, 28025-013) and random hexamers according to the manufacturer's protocols. Quantitative polymerase chain reactions (PCRs) were performed with SYBR Green Master Mix (Roche). Relative mRNA levels were determined in triplicate for each transcript using the manufacturer's software (Advanced Relative Quantification with Roche LightCycler 480 Software version 1.5) using Tubb5 transcript levels for normalization. The primers used for gene expression analyses are listed below.

No.	Transcript name	Forward (5′-3′)	Reverse (5′-3′)
1	*Pou5f1*	GCTCACCCTGGGCGTTCTC	GGCCGCAGCTTACACATGTTC
2	*Klf4*	CAGGCTGTGGCAAAACCTAT	CGTCCCAGTCACAGTGGTAA
3	*Nanog*	AAGTACCTCAGCCTCCAGCA	GTGCTGAGCCCTTCTGAATC
4	*Sox2*	AGGGCTGGGAGAAAGAAGAG	ATCTGGCGGAGAATAGTTGG
5	*Esrrb*	GAACACTCTCGCCTGGTAGG	CGCCTCCAGGTTCTCAATGT

Southern blot analyses

Genomic DNA was isolated from desired clones and digested with Bam H1-HF overnight. The digested DNA was run on a 1% agarose gel and transferred using the capillary transfer method. The clones were analyzed for targeting using an internal probe against ChR. This 809–base pair (bp) probe was amplified by PCR from the targeting vector using the following PCR primers: 5′-tcctggtccctgaggatcaa-3′ (forward) and 5′-gcggaacggagatcgaggtc-3′ (reverse). To check the correct targeting of the 5′ end, an 865-bp external probe was generated by digesting a vector containing the Rosa26 promoter (pROSA26-promoter; Addgene, no. 21710) with Sac I and Kpn 1.

Immunostaining

Cells were fixed with 4% paraformaldehyde for 20 min and then solubilized with 0.1% Triton X. After serum blocking, the cells were incubated at 4°C overnight with the primary antibody. The following day, the secondary antibody was administered for 2 hours at room temperature. Primary antibodies included anti-Oct4 (Abcam, 1:200) and anti-sarcomeric α-actinin antibody (Abcam, 1:400). Secondary antibodies, used at a 1:200 dilution, were goat anti-rabbit Texas Red (Invitrogen) and goat anti-mouse Alexa Fluor 488 (Invitrogen). NMJs were inhibited and stained in live or fixed cultures with Alexa Fluor 647–conjugated αBTX (Invitrogen) for 20 min in medium at a concentration of 5 $\mu g\ ml^{-1}$. Counterstaining was performed with 4′,6-diamidino-2-phenylindole (Invitrogen, 1:1000).

Electrophysiological assay

For the patch clamp recordings, the FACS-sorted $Hb9^{GFP+}/ChR^{tdTom+}$ MNs were plated on primary mouse cortical glial cells (Supplementary Materials). The glial cells were plated at a density of 1×10^4 cells cm^{-2} on PDL-coated 35-mm Petri dishes and allowed to reach confluency. Recordings were conducted on days 3, 10, and 16 after plating. The $Hb9^{GFP+}/ChR^{tdTom+}$ MNs were identified under a conventional inverted epifluorescence microscope (Axio Observer.A1, Zeiss) with a 20× objective lens [Plan-Neofluar; numerical aperture (NA), 0.4; Zeiss]. The formulation of the recording solutions was taken from past literature (*64*). The bath solution consisted of 145 mM NaCl, 5 mM KCl, 10 mM HEPES, 2 mM $CaCl_2$, 10 mM glucose, and 2 mM $MgCl_2$ (pH 7.3 adjusted with NaOH, 325 mOsm adjusted with sucrose). The patch pipette solution contained 130 mM CH_3KO_3S, 10 mM CH_3NaO_3S, 1 mM $CaCl_2$, 10 mM EGTA, 10 mM HEPES, 5 mM Mg–adenosine triphosphate, and 0.5 mM Na_2–guanosine triphosphate (pH 7.3, 315 mOsm). The resistance of the electrodes was 4 to 8 megohms. Patch clamp experiments were performed using a Multiclamp 700B amplifier (Axon), and signals were digitized at 10 kHz with an Axon Digidata 1440A interface. Data were acquired with pClamp 10 software (Axon) and processed with MATLAB (MathWorks). For all voltage clamp experiments, the cells were held at a membrane potential of −60 mV. APs were recorded while holding the neurons to approximately −60 mV by injecting current with amplitudes no less than −300 pA. All recordings were conducted at room temperature.

Optical and electrical stimulation

All optical stimulations were performed using a SOLA light engine (Lumencor) excitation unit, with emission peaks of interest located at 470 and 540 to 550 nm. Blue and green lights were supplied through Zeiss filter sets #38 (BP 470/40) and #20 (BP 546/12), respectively. Unless otherwise stated, the entire field of view was illuminated.

For the electrophysiological recordings, light was controlled by the Clampex software and applied through the 20× objective, yielding a maximum irradiance of 9 mW mm^{-2} as measured by a power meter (Newport) at the sample plane. The optical stimulations of the myofibers and MNs in adherent and microfluidic cultures were conducted through a 10× objective, yielding an irradiance of 7.6 mW mm^{-2} and controlled via an Arduino circuit board. Electrical stimulation was delivered via platinum electrodes positioned 3 mm away from each other across the neuromuscular tissue and controlled by an Arduino circuit delivering 9-V square inputs.

Image acquisition and analysis

Epifluorescence and confocal images were acquired on a Nikon Eclipse Ti-E inverted microscope and an Olympus FV-1000 confocal microscope, respectively. 3D reconstruction and analysis of confocal images were performed with the software Imaris (Bitplane). Automated tracking of the local deformation of the skeletal muscle cells and deflection of the pillars upon light excitation was carried out using the tracking software Tracker (http://physlets.org/tracker). The synchronization of deformation tracking and optical stimulation was carried out by plotting the average pixel intensity for every image over time and comparing the increase of intensity to the muscle or pillar deformation curve (fig. S3A). The blue bars correspond to periods of time when the light was on.

Image analysis for muscle width and axon outgrowth was conducted in ImageJ (http://imagej.nih.gov/). Maximum neurite growth rate was defined as the speed of extension of the longest neurite with respect to the border of the EB on seeding day. Electrophysiology and FACS data were processed in MATLAB (MathWorks).

Statistical analysis

Statistical analysis was conducted in GraphPad Prism (GraphPad Software Inc.). Statistical significance analysis was done via *t* tests or one-way analysis of variance (ANOVA), and all tests resulting in a *P* value less than 0.05 were considered statistically significant.

SUPPLEMENTARY MATERIALS

Supplementary material for this article is available at http://advances.sciencemag.org/cgi/content/full/2/8/e1501429/DC1

Supplementary Materials and Methods

fig. S1. DNA construct design, ESC colony morphology, DNA integration validation, and pluripotency characterization.

fig. S2. Electrophysiological characterization of the ChR-HBG3-MN.

fig. S3. Optogenetic activation of NMJs in adherent cocultures.

fig. S4. Modes of tissue ablation.

fig. S5. Photosensitization of the C2C12 myoblasts.

fig. S6. Influence of the hydrogel on the force measured by the pillar.

fig. S7. Motor neurite outgrowth in the microfluidic device.

fig. S8. Opposite gradients as a mean to provide cell-specific medium.

movie S1. Muscle contraction upon optical stimulation of ChR-HBG3-MN in adherent cultures.

movie S2. ECM compaction and muscle bundle formation over the first 96 hours of the experiment.

movie S3. 3D neurite outgrowth in the gel region bridging the neurosphere and the muscle strip.

movie S4. Muscle bundle contraction upon light simulation of the ChR-HBG3-MN in the microfluidic device.

REFERENCES AND NOTES

1. J. Olesen, A. Gustavsson, M. Svensson, H.-U. Wittchen, B. Jönsson; CDBE2010 study group, European Brain Council, The economic cost of brain disorders in Europe. *Eur. J. Neurol.* **19**, 155–162 (2012).
2. H. H. Dale, W. Feldberg, M. Vogt, Release of acetylcholine at voluntary motor nerve endings. *J. Physiol.* **86**, 353–380 (1936).
3. P. Fatt, B. Katz, Spontaneous subthreshold activity at motor nerve endings. *J. Physiol.* **117**, 109–128 (1952).
4. J. R. Sanes, J. W. Lichtman, Development of the vertebrate neuromuscular junction. *Annu. Rev. Neurosci.* **22**, 389–442 (1999).
5. G. Cao, C.-P. Ko, Schwann cell-derived factors modulate synaptic activities at developing neuromuscular synapses. *J. Neurosci.* **27**, 6712–6722 (2007).
6. H. Keshishian, K. Broadie, A. Chiba, M. Bate, The drosophila neuromuscular junction: A model system for studying synaptic development and function. *Annu. Rev. Neurosci.* **19**, 545–575 (1996).
7. E. M. Jorgensen, M. L. Nonet, Neuromuscular junctions in the nematode *C. elegans*. *Dev. Biol.* **6**, 207–220 (1995).
8. J. L. Cohen, K. R. Weiss, I. Kupfermann, Motor control of buccal muscles in Aplysia. *J. Neurophysiol.* **41**, 157–180 (1978).
9. E. Frank, G. D. Fischbach, Early events in neuromuscular junction formation in vitro: Induction of acetylcholine receptor clusters in the postsynaptic membrane and morphology of newly formed synapses. *J. Cell Biol.* **83**, 143–158 (1979).
10. E. M. Ullian, B. T. Harris, A. Wu, J. R. Chan, B. A. Barres, Schwann cells and astrocytes induce synapse formation by spinal motor neurons in culture. *Mol. Cell. Neurosci.* **25**, 241–251 (2004).
11. L. L. Rubin, S. M. Schuetze, C. L. Weill, G. D. Fischbach, Regulation of acetylcholinesterase appearance at neuromuscular junctions in vitro. *Nature* **283**, 264–267 (1980).
12. X.-J. Li, Z.-W. Du, E. D. Zarnowska, M. Pankratz, L. O. Hansen, R. A. Pearce, S.-C. Zhang, Specification of motoneurons from human embryonic stem cells. *Nat. Biotechnol.* **23**, 215–221 (2005).
13. G. B. Miles, D. C. Yohn, H. Wichterle, T. M. Jessell, V. F. Rafuse, R. M. Brownstone, Functional properties of motoneurons derived from mouse embryonic stem cells. *J. Neurosci.* **24**, 7848–7858 (2004).
14. P. H. Chipman, Y. Zhang, V. F. Rafuse, A stem-cell based bioassay to critically assess the pathology of dysfunctional neuromuscular junctions. *PLOS One* **9**, e91643 (2014).
15. M. Das, J. W. Rumsey, C. A. Gregory, N. Bhargava, J.-F. Kang, P. Molnar, L. Riedel, X. Guo, J. J. Hickman, Embryonic motoneuron-skeletal muscle co-culture in a defined system. *Neuroscience* **146**, 481–488 (2007).
16. X. Guo, M. Das, J. Rumsey, M. Gonzalez, M. Stancescu, J. Hickman, Neuromuscular junction formation between human stem-cell-derived motoneurons and rat skeletal muscle in a defined system. *Tissue Eng. Part C Methods* **16**, 1347–1355 (2010).
17. J. A. Umbach, K. L. Adams, C. B. Gundersen, B. G. Novitch, Functional neuromuscular junctions formed by embryonic stem cell-derived motor neurons. *PLOS One* **7**, e36049 (2012).
18. A. J. Engler, M. A. Griffin, S. Sen, C. G. Bönnemann, H. L. Sweeney, D. E. Discher, Myotubes differentiate optimally on substrates with tissue-like stiffness: Pathological implications for soft or stiff microenvironments. *J. Cell Biol.* **166**, 877–887 (2004).
19. R. K. Willits, S. L. Skornia, Effect of collagen gel stiffness on neurite extension. *J. Biomater. Sci. Polym. Ed.* **15**, 1521–1531 (2004).
20. H. G. Sundararaghavan, G. A. Monteiro, B. L. Firestein, D. I. Shreiber, Neurite growth in 3D collagen gels with gradients of mechanical properties. *Biotechnol. Bioeng.* **102**, 632–643 (2009).
21. J. R. Sanes, Roles of extracellular matrix in neural development. *Annu. Rev. Physiol.* **45**, 581–600 (1983).
22. D. A. Tonge, J. P. Golding, M. Edbladh, M. Kroon, P. E. R. Ekström, A. Edström, Effects of extracellular matrix components on axonal outgrowth from peripheral nerves of adult animals in vitro. *Exp. Neurol.* **146**, 81–90 (1997).
23. R. B. Campenot, K. Lund, S.-A. Mok, Production of compartmented cultures of rat sympathetic neurons. *Nat. Protoc.* **4**, 1869–1887 (2009).
24. P. G. Nelson, R. D. Fields, C. Yu, Y. Liu, Synapse elimination from the mouse neuromuscular junction in vitro: A non-Hebbian activity-dependent process. *J. Neurobiol.* **24**, 1517–1530 (1993).
25. J. M. Harper, C. Krishnan, J. S. Darman, D. M. Deshpande, S. Peck, I. Shats, S. Backovic, J. D. Rothsein, D. A. Kerr, Axonal growth of embryonic stem cell-derived motoneurons in vitro and in motoneuron-injured adult rats. *Proc. Natl. Acad. Sci. U.S.A.* **101**, 7123–7218 (2004).
26. A. Takeuchi, S. Nakafutami, H. Tani, M. Mori, Y. Takayama, H. Moriguchi, K. Kotani, K. Miwa, J. Lee, M. Noshinori, Y. Jimbo, Device for co-culture of sympathetic neurons and cardiomyocytes using microfabrication. *Lab Chip* **11**, 2268–2275 (2011).
27. A. Takeuchi, K. Shimba, M. Mori, Y. Takayama, H. Moriguchi, K. Kotani, J.-K. Lee, M. Noshiro, Y. Jimbo, Sympathetic neurons modulate the beat rate of pluripotent cell-derived cardiomyocytes in vitro. *Integr. Biol.* **4**, 1532–1539 (2012).
28. Z. Tong, O. Seira, C. Casas, D. Reginensi, A. Homs-Corbera, J. Samitier, J. A. Del Rio, Engineering a functional neuro-muscular junction model in a chip. *RSC Adv.* **4**, 54788–54797 (2014).
29. K. A. Southam, A. E. King, C. A. Blizzard, G. H. McCormack, T. C. Dickson, Microfluidic primary culture model of the lower motor neuron-neuromuscular junction circuit. *J. Neurosci. Methods* **218**, 164–169 (2013).
30. E. E. Zahavi, A. Ionescu, S. Gluska, T. Gradus, K. Ben-Yaakov, E. Perlson, A compartmentalized microfluidic neuromuscular co-culture system reveals spatial aspects of GDNF functions. *J. Cell Sci.* **128**, 1241–1252 (2015).
31. A. Ionescu, E. E. Zahavi, T. Gradus, K. Ben-Yaakov, E. Perlson, Compartmental microfluidic system for studying muscle–neuron communication and neuromuscular junction maintenance. *Eur. J. Cell Biol.* **95**, 69–88 (2016).
32. A. D. Bach, J. P. Beier, G. B. Stark, Expression of Trisk 51, agrin and nicotinic-acetycholine receptor ε-subunit during muscle development in a novel three-dimensional muscle-neuronal co-culture system. *Cell Tissue Res.* **314**, 263–274 (2003).
33. S. Hinds, W. Bian, R. G. Dennis, N. Bursac, The role of extracellular matrix composition in structure and function of bioengineered skeletal muscle. *Biomaterials* **32**, 3575–3583 (2011).
34. H. H. Vandenburgh, M. Del Tatto, J. Shansky, J. Lemaire, A. Chang, F. Payumo, P. Lee, A. Goodyear, L. Raven, Tissue-engineered skeletal muscle organoids for reversible gene therapy. *Hum. Gene Ther.* **7**, 2195–2200 (1996).
35. Y. Morimoto, M. Kato-Negishi, H. Onoe, S. Takeuchi, Three-dimensional neuron–muscle constructs with neuromuscular junctions. *Biomaterials* **34**, 9413–9419 (2013).
36. K. R. Tan, M. Brown, G. Labouèbe, C. Yvon, C. Creton, J.-M. Fritschy, U. Rudolph, C. Lüscher, Neural bases for addictive properties of benzodiazepines. *Nature* **463**, 769–774 (2010).
37. A. W. Feinberg, A. Feigel, S. S. Shevkoplyas, S. Sheehy, G. M. Whitesides, K. K. Parker, Muscular thin films for building actuators and powering devices. *Science* **317**, 1366–1370 (2007).
38. C. W. McAleer, A. S. T. Smith, S. Najjar, K. Pirozzi, C. J. Long, J. J. Hickman, Mechanistic investigation of adult myotube response to exercise and drug treatment in vitro using a multiplexed functional assay system. *J. Appl. Physiol.* **117**, 1398–1405 (2014).
39. K. Wilson, M. Das, K. J. Wahl, R. J. Colton, J. Hickman, Measurement of contractile stress generated by cultured rat muscle on silicon cantilevers for toxin detection and muscle performance enhancement. *PLOS One* **5**, e11042 (2010).
40. A. S. T. Smith, C. J. Long, K. Pirozzi, J. J. Hickman, A functional system for high-content screening of neuromuscular junctions in vitro. *Technology* **1**, 37–48 (2013).
41. V. Vickerman, J. Blundo, S. Chung, R. Kamm, Design, fabrication and implementation of a novel multi-parameter control microfluidic platform for three-dimensional cell culture and real-time imaging. *Lab Chip* **8**, 1468–1477 (2008).
42. Y. Shin, S. Han, J. S. Jeon, K. Yamamoto, I. K. Zervantonakis, R. Sudo, R. D. Kamm, S. Chung, Microfluidic assay for simultaneous culture of multiple cell types on surfaces or within hydrogels. *Nat. Protoc.* **7**, 1247–1259 (2012).
43. B. Mosadegh, C. Huang, J. W. Park, H. S. Shin, B. G. Chung, S.-K. Hwang, K.-H. Lee, H. J. Kim, J. Brody, N. L. Jeon, Generation of stable complex gradients across two-dimensional surfaces and three-dimensional gels. *Langmuir* **23**, 10910–10912 (2007).
44. H. Vandenburgh, J. Shansky, F. Benesch-Lee, V. Barbata, J. Reid, L. Thorrez, R. Valentini, G. Crawford, Drug-screening platform based on the contractility of tissue-engineered muscle. *Muscle Nerve* **37**, 438–447 (2008).
45. W. R. Legant, A. Pathak, M. T. Yang, V. S. Deshpande, R. M. McMeeking, C. S. Chen, Microfabricated tissue gauges to measure and manipulate forces from 3D microtissues. *Proc. Natl. Acad. Sci. U.S.A.* **106**, 10097–10102 (2009).
46. S. G. M. Uzel, A. Pavesi, R. D. Kamm, Microfabrication and microfluidics for muscle tissue models. *Prog. Biophys. Mol. Biol.* **115**, 279–293 (2014).
47. G. Nagel, T. Szellas, W. Huhn, S. Kateriya, N. Adeishvili, P. Berthold, D. Ollig, P. Hegemann, E. Bamberg, Channelrhodopsin-2, a directly light-gated cation-selective membrane channel. *Proc. Natl. Acad. Sci. U.S.A.* **100**, 13940–13945 (2003).
48. E. S. Boyden, F. Zhang, E. Bamberg, G. Nagel, K. Deisseroth, Millisecond-timescale, genetically targeted optical control of neural activity. *Nat. Neurosci.* **8**, 1263–1268 (2005).
49. S. R. Pulver, S. L. Pashkovski, N. J. Hornstein, P. A. Garrity, L. C. Griffith, Temporal dynamics of neuronal activation by channelrhodopsin-2 and TRPA1 determine behavioral output in *Drosophila* larvae. *J. Neurophysiol.* **101**, 3075–3088 (2009).
50. M. E. Llewellyn, K. R. Thompson, K. Deisseroth, S. L. Delp, Orderly recruitment of motor units under optical control in vivo. *Nat. Med.* **16**, 1161–1165 (2010).

51. V. Caggiano, M. Sur, E. Bizzi, Rostro-caudal inhibition of hindlimb movements in the spinal cord of mice. *PLOS One* **9**, e100865 (2014).
52. C. Schroll, T. Riemensperger, D. Bucher, J. Ehmer, T. Völler, K. Erbguth, B. Gerber, T. Hendel, G. Nagel, E. Buchner, A. Fiala, Light-induced activation of distinct modulatory neurons triggers appetitive or aversive learning in *Drosophila* larvae. *Curr. Biol.* **16**, 1741–1747 (2006).
53. J. B. Bryson, C. B. Machado, M. Crossley, D. Stevenson, V. Bros-Facer, J. Burrone, L. Greensmith, I. Lieberam, Optical control of muscle function by transplantation of stem cell–derived motor neurons in mice. *Science* **344**, 94–97 (2014).
54. J. A. Steinbeck, M. K. Jaiswal, E. L. Calder, S. Kishinevsky, A. Weishaupt, K. V. Toyka, P. A. Goldstein, L. Studer, Functional connectivity under optogenetic control allows modeling of human neuromuscular disease. *Cell Stem Cell* **18**, 134–143 (2016).
55. H. Wichterle, M. Peljto, Differentiation of mouse embryonic stem cells to spinal motor neurons. *Curr. Protoc. Stem Cell Biol.* **Chapter 1**, Unit 1H.1.1–1H.1.9 (2008).
56. J. P. Weick, M. A. Johnson, S. P. Skroch, J. C. Williams, K. Deisseroth, S.-C. Zhang, Functional control of transplantable human ESC-derived neurons via optogenetic targeting. *Stem Cells* **28**, 2008–2016 (2010).
57. M. S. Sakar, D. Neal, T. Boudou, M. A. Borochin, Y. Li, R. Weiss, R. D. Kamm, C. S. Chen, H. H. Asada, Formation and optogenetic control of engineered 3D skeletal muscle bioactuators. *Lab Chip* **12**, 4976–4985 (2012).
58. T. Asano, T. Ishizua, H. Yawo, Optically controlled contraction of photosensitive skeletal muscle cells. *Biotechnol. Bioeng.* **109**, 199–204 (2012).
59. H. Wichterle, I. Lieberam, J. A. Porter, T. M. Jessell, Directed differentiation of embryonic stem cells into motor neurons. *Cell* **110**, 385–397 (2002).
60. R. Pittier, F. Sauthier, J. A. Hubbell, H. Hall, Neurite extension and in vitro myelination within three-dimensional modified fibrin matrices. *J. Neurobiol.* **63**, 1–14 (2005).
61. T. Wada, M. Honda, I. Minami, N. Tooi, Y. Amagai, N. Nakatsuji, K. Aiba, Highly efficient differentiation and enrichment of spinal motor neurons derived from human and monkey embryonic stem cells. *PLOS One* **4**, e6722 (2009).
62. A. D. Ebert, J. Yu, F. F. Rose Jr., V. B. Mattis, C. L. Lorson, J. A. Thomson, C. N. Svendsen, Induced pluripotent stem cells from a spinal muscular atrophy patient. *Nature* **457**, 277–280 (2009).
63. J. T. Dimos, K. T. Rodolfa, K. K. Niakan, L. M. Weisenthal, H. Mitsumoto, W. Chung, G. F. Croft, G. Saphier, R. Leibel, R. Goland, H. Wichterle, C. E. Henderson, K. Eggan, Induced pluripotent stem cells generated from patients with ALS can be differentiated into motor neurons. *Science* **321**, 1218–1221 (2008).
64. E. O. Mazzoni, S. Mahony, M. Closser, C. A. Morrison, S. Nedelec, D. J. Williams, D. An, D. K. Gifford, H. Wichterle, Synergistic binding of transcription factors to cell-specific enhancers programs motor neuron identity. *Nat. Neurosci.* **16**, 1219–1227 (2013).
65. M. E. Hester, M. J. Murtha, S. Song, M. Rao, C. J. Miranda, K. Meyer, J. Tian, G. Boulting, D. V. Schaffer, M. X. Zhu, S. L. Pfaff, F. H. Gage, B. K. Kaspar, Rapid and efficient generation of functional motor neurons from human pluripotent stem cells using gene delivered transcription factor codes. *Mol. Ther.* **19**, 1905–1912 (2011).
66. O. Yizhar, L. E. Fenno, T. J. Davidson, M. Mogri, K. Deisseroth, Optogenetics in neural systems. *Neuron* **71**, 9–34 (2011).
67. A.-S. Arnold, J. Gill, M. Christe, R. Ruiz, S. McGuirk, J. St-Pierre, L. Tabares, C. Handschin, Morphological and functional remodelling of the neuromuscular junction by skeletal muscle PGC-1α. *Nat. Commun.* **5**, 3569 (2014).
68. R. M. Fitzsimonds, M.-M. Poo, Retrograde signaling in the development and modification of synapses. *Physiol. Rev.* **78**, 143–170 (1998).
69. R. M. Wyatt, R. J. Balice-Gordon, Activity-dependent elimination of neuromuscular synapses. *J. Neurocytol.* **32**, 777–794 (2003).
70. J. C. Nawroth, H. Lee, A. W. Feinberg, C. M. Ripplinger, M. L. McCain, A. Grosberg, J. O. Dabiri, K. K. Parker, A tissue-engineered jellyfish with biomimetic propulsion. *Nat. Biotechnol.* **30**, 792–797 (2012).
71. C. Cvetkovic, R. Raman, V. Chan, B. J. Williams, M. Tolish, P. Bajaj, M. S. Sakar, H. H. Asada, M. T. A. Saif, R. Bashir, Three-dimensionally printed biological machines powered by skeletal muscle. *Proc. Natl. Acad. Sci. U.S.A.* **111**, 10125–10130 (2014).
72. B. J. Williams, S. V. Anand, J. Rajagopalan, M. T. A. Saif, A self-propelled biohybrid swimmer at low Reynolds number. *Nat. Commun.* **5**, 3081 (2014).
73. V. Chan, K. Park, M. B. Collens, H. Kong, T. A. Saif, R. Bashir, Development of miniaturized walking biological machines. *Sci. Rep.* **2**, 857 (2012).
74. R. Raman, C. Cvetkovic, S. G. M. Uzel, R. J. Platt, P. Sengupta, R. D. Kamm, R. Bashir, Optogenetic skeletal muscle-powered adaptive biological machines. *Proc. Natl. Acad. Sci. U.S.A.* **113**, 3497–3502 (2016).
75. D. Bonanomi, S. L. Pfaff, Motor axon pathfinding. *Cold Spring Harb. Perspect. Biol.* **2**, a001735 (2010).
76. S. Nédelec, M. Peljto, P. Shi, M. W. Amoroso, L. C. Kam, H. Wichterle, Concentration-dependent requirement for local protein synthesis in motor neuron subtype-specific response to axon guidance cues. *J. Neurosci.* **32**, 1496–1506 (2012).
77. A. Ebens, K. Brose, E. D. Leonardo, M. G. Hanson Jr., F. Bladt, C. Birchmeier, B. A. Barres, M. Tessier-Lavigne, Hepatocyte growth factor/scatter factor is an axonal chemoattractant and a neurotrophic factor for spinal motor neurons. *Neuron* **17**, 1157–1172 (1996).
78. S. Gensler, A. Sander, A. Korngreen, G. Traina, G. Giese, V. Witzemann, Assembly and clustering of acetylcholine receptors containing GFP-tagged ε or γ subunits: Selective targeting to the neuromuscular junction in vivo. *Eur. J. Biochem.* **268**, 2209–2217 (2001).
79. O. L. Gervásio, W. D. Phillips, Increased ratio of rapsyn to ACh receptor stabilizes postsynaptic receptors at the mouse neuromuscular synapse. *J. Physiol.* **562** (Pt. 3), 673–685 (2005).
80. S. R. Thomson, T. M. Wishart, R. Patani, S. Chandran, T. H. Gillingwater, Using induced pluripotent stem cells (iPSC) to model human neuromuscular connectivity: Promise or reality? *J. Anat.* **220**, 122–130 (2012).
81. D. Neal, M. S. Sakar, L.-L. S. Ong, H. H. Asada, Formation of elongated fascicle-inspired 3D tissues consisting of high-density, aligned cells using sacrificial outer molding. *Lab Chip* **14**, 1907–1916 (2014).
82. V. Chan, D. M. Neal, S. G. M. Uzel, H. Kim, R. Bashir, H. H. Asada, Fabrication and characterization of optogenetic, multi-strip cardiac muscles. *Lab Chip* **15**, 2258–2268 (2015).
83. M. Juhas, G. C. Engelmayr Jr., A. N. Fontanella, G. M. Palmer, N. Bursac, Biomimetic engineered muscle with capacity for vascular integration and functional maturation in vivo. *Proc. Natl. Acad. Sci. U.S.A.* **111**, 5508–5513 (2014).
84. Y.-J. Son, W. J. Thompson, Schwann cell processes guide regeneration of peripheral axons. *Neuron* **14**, 125–132 (1995).
85. R. A. C. Hughes, D. R. Cornblath, Guillain-Barré syndrome. *Lancet* **366**, 1653–1666 (2005).
86. A. S. D. Saporta, S. L. Sottile, L. J. Miller, S. M. E. Feely, C. E. Siskind, M. E. Shy, Charcot-Marie-Tooth disease subtypes and genetic testing strategies. *Ann. Neurol.* **69**, 22–33 (2011).
87. H. Vandenburgh, High-content drug screening with engineered musculoskeletal tissues. *Tissue Eng. Part B Rev.* **16**, 55–64 (2010).
88. C. Luni, E. Serena, N. Elvassore, Human-on-chip for therapy development and fundamental science. *Curr. Opin. Biotechnol.* **25**, 45–50 (2014).
89. D. Yaffe, O. Saxel, Serial passaging and differentiation of myogenic cells isolated from dystrophic mouse muscle. *Nature* **270**, 725–727 (1977).

Acknowledgments: We thank H. Wichterle and T. Jessell for sharing the ES cell line HBG3 and to L. Wood for providing the glial feeder cells and insightful comments during manuscript preparation. We thank F. Zhang for providing resources and access to equipment for this project. We are also grateful to W. Li, K. Broderick, and T. Honegger for their guidance in microfabrication; N. Sanjana, J. Lefkowitz, and J. Pan for their training at electrophysiology and for making their scope available to us; and the Stice, Bashir, Saif, Gillette, Weiss, and Chen laboratories, together with D. Williams and J. Lichtman, for the insightful discussions. The help from M. Griffin and M. Jennings at the Koch Institute flow cytometry facility was greatly appreciated. We are grateful to S. Sakar and D. Neal for inspiring this study. We also thank N. Hammond and all the manuscript readers for their useful comments. **Funding:** S.G.M.U., V.S., and V.C. are grateful to the funding from the NSF Science and Technology Center for Emergent Behaviors of Integrated Cellular Systems (CBET-0939511). R.J.P. is supported by an NSF Graduate Research Fellowship under grant no. 1122374. C.J.R. is grateful for a Wellcome Trust MIT Postdoctoral Research Fellowship to carry out this research; this work was supported by the Wellcome Trust 093831/Z/10/Z. R.D.K. would like to acknowledge the following funding sources: National Research Foundation, Singapore-MIT Alliance for Research and Technology, and BioSystems and Micromechanics (BioSyM) IRG. **Author contributions:** S.G.M.U. designed the experiments and the microfluidic platform, created the cell line, conducted the experiments, analyzed the data, and prepared the manuscript. R.J.P. designed and fabricated the DNA construct, contributed to the cell line creation, and edited the manuscript. V.S. performed the molecular biology assays, contributed to the cell line creation, and edited the manuscript. T.M.P. conducted experiments and data analysis. C.J.R. built the laser ablation platform. V.C. performed the pillar stiffness measurement. L.A.B., P.T.C.S., and R.D.K. supervised the study and participated in the preparation of the manuscript. **Competing interests:** R.D.K. is a cofounder of AIM Biotech and has financial interest in this company. **Data and materials availability:** All data used to obtain the conclusions in this paper are present in the paper and/or the Supplementary Materials. Additional data related to this paper may be requested from the authors.

Submitted 12 October 2015
Accepted 6 July 2016
Published 3 August 2016
10.1126/sciadv.1501429

Citation: S. G. M. Uzel, R. J. Platt, V. Subramanian, T. M. Pearl, C. J. Rowlands, V. Chan, L. A. Boyer, P. T. C. So, R. D. Kamm, Microfluidic device for the formation of optically excitable, three-dimensional, compartmentalized motor units. *Sci. Adv.* **2**, e1501429 (2016).

Microfluidic device for the formation of optically excitable, three-dimensional, compartmentalized motor units

Sebastien G. M. Uzel, Randall J. Platt, Vidya Subramanian, Taylor M. Pearl, Christopher J. Rowlands, Vincent Chan, Laurie A. Boyer, Peter T. C. So and Roger D. Kamm

Sci Adv **2** (8), e1501429.
DOI: 10.1126/sciadv.1501429